PHYSICAL REVIEW E **80**, 021504 (2009)

Rheology of draining steady-state foams

Raenell Soller and Stephan A. Koehler[*]
Department of Physics, WPI, Worcester, Massachusetts 01609, USA

(Received 27 September 2008; revised manuscript received 31 March 2009; published 20 August 2009)

Aqueous foams continuously age due to fluid drainage and bubble coarsening, which makes it difficult to perform steady-state rheological measurements. Consequently we have developed the foam drainage rheology technique, where perfusion counteracts fluid drainage and bubble replenishment counteracts bubble coarsening during measurement of the shear stresses by a rheometer. We evaluate published power-law and Herschel-Bulkley models and find that parameters derived from emulsion experiments cannot describe our results. We propose a hybrid model, which combines our earlier film-shearing model, where the film thickness depends on liquid volume fraction, with a Herschel-Bulkley shear-rate dependence.

DOI: 10.1103/PhysRevE.80.021504 PACS number(s): 46.35.+z, 47.57.−s, 83.80.Iz

I. INTRODUCTION

Aqueous foams are a class of disordered soft material that has received a lot of scientific attention because despite their simple composition (merely gas bubbles packed in water) they exhibit a rich variety of dynamical and mechanical behaviors [1–3]. These include aging, which is due to the combined effects of fluid drainage [4,5] and bubble coarsening [6,7] that are often coupled [8–10]. Although drainage and coarsening are fairly well understood for certain surfactant systems [11–13], the shearing behavior of foams remains poorly understood [14]. One outstanding question is how energy is dissipated during shearing [15] because it is a complex process that spans several orders of magnitude in size from motion of surfactant molecules to large scale motion of bubbles. On the experimental side, steady-state rheological measurements are problematic because the time scales of the aging processes are often comparable to those of measurements [16,17]. Thus despite their apparent simplicity, foams have a complex phenomenology and continue to present a broad range of challenges for the scientific community spanning physics and engineering. Moreover, it is precisely this rich diversity of behaviors that has allowed for a plethora of different uses of foams in industry, such as minerals separation, water purification, and advanced oil extraction [2,18,19].

Stable foams with low fluid content that are slowly sheared at small amplitudes can be modeled with reasonable success based on perturbations of the surface area, which is proportional to the surface energy [16,20–22]. However outside this limiting case the physics becomes complicated. At increased shearing amplitudes, bubbles rearrange quickly [23], thereby invalidating perturbation approaches. Additionally, the foam's fluid content has a large effect on shearing behavior; as the liquid volume fraction increases the bubbles spontaneously rearrange [24] and at the critical liquid volume fraction, $\epsilon_c \approx 0.36$, both the elastic and loss moduli vanish [17,25–28]. Moreover, inertial, viscous, and interfacial effects such as Marangoni stresses and surface viscosity become important at faster shear rates [15,29,30]. Given that all these complexities impede theoretical treatment, only a synthesis of careful experimental and theoretical work can lead to a complete understanding of foam rheology.

On longer time scales the metastability of foam manifests itself through aging processes, which principally are coarsening and drainage. Coarsening refers to the growth of bubbles due to preferential gas diffusion across thin liquid films from smaller bubbles to larger bubbles. Smaller bubbles shrink and disappear, leaving behind coarser (i.e., larger) bubbles. Drainage refers to the flow of liquid due to capillary and gravitational forces. Both processes minimize energy: the former minimizes surface energy by reducing the interfacial surface area, whereas drainage lowers the gravitational potential energy. In general drainage and coarsening couple to produce a positive feedback loop that minimizes energy [9]: drainage removes liquid which enhances diffusion between bubbles and coarsening enlarges the channels which enhances drainage. Additionally, coarsening affects shearing [31] and vice versa [32], and it may be natural to expect sheared foams to drain differently than unsheared foams given that granular materials dilate [33] upon shearing. Although considerable progress has been made regarding drainage [4,5,11,34,35], coarsening [6,12,13,36], and their couplings [9,37], many fundamental aspects of foam rheology remain poorly understood [14].

A major experimental challenge for rheologists is that foams generally evolve during measurements [17,27]. For example, wet foams drain quickly and foams with small bubbles coarsen rapidly, which make steady-state measurements difficult if not impossible. Experimentalists have resolved the drainage issue using two different methods. One option is using fluids with high viscosities to diminish the drainage rate [17]. But increasing the bulk viscosity diminishes the interfacial rigidity, which is characterized by the Boussinesq number $\mathrm{Bo} = \mu_s / \mu L$, and therefore affects rheological behavior [29]. A second workaround is using concentrated emulsions (which are also known as liquid-liquid foams) because they have identical geometry but drain and coarsen much slower. Since the two phases have similar densities (unlike water and air), buoyancy effects lead to much reduced drainage rates [38]. Moreover the diffusive transport of the dispersed phase (e.g., oil) through the continuous phase (e.g., water) is also very slow. Despite their striking geometric similarity, emulsions and foams differ in terms of

---

[*] sak@wpi.edu

their dynamics: Earth-bound foams always drain and their films are almost always in motion. If drainage flow couples to shear flow, then emulsions are not a suitable general proxy for foams, which necessitates direct rheological measurements of draining foams.

In this work we examine the fluidlike behavior by continuously shearing foams using our recently developed foam drainage rheology (FDR) technique [39]. By continuously regenerating the foam we prevent coarsening from affecting the measurements and by fluid perfusion (i.e., replenishment) we fix the liquid fraction and prevent drainage from adversely affecting the measurements. Rather than only changing the shear rate, as is done using conventional methods, we have introduced an additonal degree of freedom, which is changing the liquid volume fraction on the fly. This allows us to determine the relationship between liquid content and shear stress in a single session.

Since the FDR technique heavily involves drainage, we briefly review drainage in Sec. I A. In particular we extend foam drainage theory for our experiments by including continuous regeneration, injection from a point source, and foam expansion due to high liquid content. In Sec. I B, we review four constitutive relations between stress and rate of strain for continuous shearing [27,30,39,40], which essentially are variants of the Herschel-Bulkley equation that differ in their treatment of the yield stress and liquid volume fraction. Section II gives experimental details of the FDR technique and in subsequent sections we simultaneously present and discuss results for a coarse and a fine soap foam. Section III A treats the self-similar nature of incremental perfusions. Section III B deals with the inverse relationship between shear stress and liquid volume fraction. We evaluate the evolution of the shear stress due to an incremental perfusion sequence in Sec. III C. Section III D gives the experimentally determined constitutive relation between shear stress, shear rate, and liquid volume fraction, which we compare with existing models and use to create a hybrid model. Section III E presents pulsed perfusions at different rates of shear and serves as a check of the rheological models. We conclude and offer suggestions for further investigations in Sec. IV.

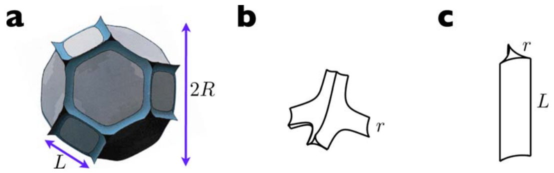

FIG. 1. (Color online) (a) A Kelvin bubble, which is an idealized foam bubble whose faces are squares and hexagons. The edge length is L and the effective bubble diameter is $R=1.393L$. (b) Closeup of a node, which is a fourfold junction. (c) An idealized channel, which has length L and radius of curvature (in the transverse direction) r.

A. Drainage

Liquid flows through foams in a tortuous fashion, which differs from flow through porous solids, such as sandstone, because the shape of the bubbles adjusts to the flow rate. Moreover, the geometry of a foam is based on surface energy minimization that leads to certain topologies for the continuous (liquid) and dispersed (gas) phases. It can be idealized as packed identical Kelvin bubbles, which are 14-sided polygons and whose equivalent radius R is based on their volume [see the sketch in Fig. 1(a)]. The continuous phase is depicted by the blue (dark gray) regions decorating the edges of the polygon. It is composed of nodes [see Fig. 1(b)] and channels (also known as Plateau borders) [see Fig. 1(c)]. Increases in drainage flow, q, are accompanied by increases in liquid volume fraction, ϵ. This results in an increasing channel width, r, as well as expansion of the foam's total volume (we are assuming isobaric conditions), which in turn increases the separation between neighboring nodes, L. Taking into account this expansion effect Neethling *et al.* [34] developed an implicit relationship for ϵ,

$$\epsilon = \delta_c\left(\frac{r}{L}\right)^2(1-\epsilon)^{2/3} + \delta_n\left(\frac{r}{L}\right)^3(1-\epsilon) \qquad (1)$$

with

$$\delta_c = 0.171, \qquad \delta_n = 0.20.$$

Similar to Darcy flow, the liquid flow rate in foams is proportional to the driving forces, which are gravity, $\rho\mathbf{g}$, and capillarity, $\nabla(\sigma/r)$, where σ is the surface tension and r is the radius of curvature of the channel [see Fig. 1(c)]. Experiments show a simple power-law relation between the average fluid velocity, u, and liquid volume fraction, ϵ, but there is quite a degree of variability in the prefactor and exponent [11,35,41]. Accordingly, the velocity can be written as

$$\mathbf{u} = \frac{KL^2\epsilon^{\chi}}{\mu}\left[\rho\mathbf{g} + \boldsymbol{\nabla}\left(\frac{\sigma}{r}\right)\right], \qquad (2)$$

where L is the edge length of the channels and K is a dimensionless prefactor, which we call the permeability prefactor. Both bubble size and surfactant type affect the two permeability constants, a fact which is only partially understood. Certain surfactants result in more rigid interfaces, whereas others result in more mobile interfaces, which may be attributed to high and low surface viscosities, respectively. For the former case the boundary condition is no slip at the channel walls, the flow is Poiseuille-like in the channels, and the permeability exponent is $\chi=1$. For the latter case the interfaces are flowing and offer little resistance to the fluid flow in the channels. The flow therefore is pluglike and the permeability exponent is $\chi \approx 1/2$. For the surfactant used in our investigation the permeability exponent is close to 1/2 and the permeability prefactor increases with diminishing bubble size—see Appendix A.

We now reformulate foam drainage theory in the context of our experiments, which involve continuous bubble generation and perfusion from a point. We denote the gas' volumetric flow rate ψ_{gas} and assume that the gas pressure inside the bubbles is atmospheric. The gas flux is proportional to the bubbles' rise velocity and the volume not taken up by liquid, $1-\epsilon$. Thus the velocity of the rising bubbles given by Eq. (2) is modified [42],

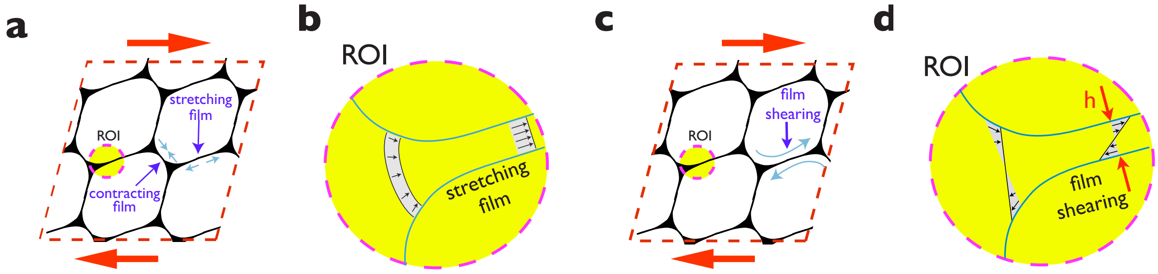

FIG. 2. (Color online) Schematics of two types of shearing mechanisms: (a) scenario of film stretching and film contraction, with the region of interest (ROI) shown in (b), which is a convergent flow due to film stretching; (c) scenario of film shearing, with the ROI shown in (d), which is shearing due to opposing interfacial flows.

$$\mathbf{u}_{\text{bubbles}} = -\psi_{\text{gas}}/(1-\epsilon)\hat{\mathbf{z}}, \tag{3}$$

where $\hat{\mathbf{z}}$ is the unit vector pointing downward in the direction of gravity. To account for the rising bubbles, the drainage velocity in the laboratory frame is

$$\mathbf{u} = \frac{KL^2\epsilon^{\chi}}{\mu}\left[\rho\mathbf{g} + \nabla\left(\frac{\sigma}{r}\right)\right] - \left(\frac{\psi_{\text{gas}}}{1-\epsilon}\right)\hat{\mathbf{z}}. \tag{4}$$

Continuity of liquid leads to the foam drainage equation,

$$\frac{\partial}{\partial t}\epsilon + \nabla\cdot\left\{\frac{KL^2\epsilon^{\chi+1}}{\mu}\left[\rho\mathbf{g} + \nabla\left(\frac{\sigma}{r}\right)\right] - \psi_{\text{gas}}\left(\frac{\epsilon}{1-\epsilon}\right)\hat{\mathbf{z}}\right\} = 0, \tag{5}$$

which describes how fluid within a foam is redistributed.

Fluid perfusion at a volumetric rate ψ_l at a point that, for convenience, is set to the origin introduces a source term to the right-hand side of Eq. (5),

$$\begin{aligned}\frac{\partial}{\partial t}\epsilon(\mathbf{x},t) + \nabla\cdot\Bigg\{&\frac{KL^2\epsilon(\mathbf{x},t)^{\chi+1}}{\mu}\left[\rho\mathbf{g} + \nabla\left(\frac{\sigma}{r(\mathbf{x},t)}\right)\right]\\ &- \psi_{\text{gas}}\left[\frac{\epsilon(\mathbf{x},t)}{1-\epsilon(\mathbf{x},t)}\right]\hat{\mathbf{z}}\Bigg\}\\ = \psi_l\delta(\mathbf{x}),\end{aligned} \tag{6}$$

where $\delta(\mathbf{x})$ is the Dirac delta function.

B. Rheology

There is little general consensus on any basic theory for rheology and, in fact, several different experimental trends have been reported, which in part is due to the dependence on bubble size, liquid distribution, as well as surfactant type. Since foams coarsen and drain over time, controlling the first two parameters during measurement adds to the challenges faced by experimentalists. Moreover, there is a wide range of rheological measurements, such as oscillatory shearing at small and large amplitudes, continuous shearing, and step-strain shearing, each of which reveals different limiting behaviors. Many details remain unknown [14,43], and thus a complete constitutive relation that takes into account material properties, such as bubble size, liquid content, and surfactant type, as well as the shearing process, is likely to be quite complex.

Several relationships between stress, τ, and steady-state shear rate, $\dot{\gamma}$, have been reported. These functionally resemble a Herschel-Bulkley fluid,

$$\tau = \tau_y + k\dot{\gamma}^n, \tag{7}$$

where τ_y is the yield stress, k is the consistency [44], and n is the power-law index. It is implied that the yield stress and consistency depend on material properties (e.g., $R,\epsilon,\mu,\sigma,\ldots$) but not on $\dot{\gamma}$. The reported values of the power-law index vary considerably, $0.2 \le n \le 1$ [14], which has, in part, been attributed to differing physicochemical properties of surfactants [29].

Early work on foam rheology was performed by groups headed by Princen [45] and also Armstrong [20]. These studies were based on the film-stretching model that shares similarities with Bretherton's analysis [46] for bubbles flowing along a wall [21] and is based on a fixed film thickness and the dilation and contraction of films that occur during shearing—see Fig. 2(a). The liquid volume of a dilating film increases, producing a convergent flow into the film [see Fig. 2(b)]. Conversely for film contraction a divergent flow out of the film occurs. In both cases the dynamics are set by a balance of the stresses, which are viscous shearing, $\mu\dot{\gamma}$, and surface tension, σ/R, in the transitional region between the Plateau border and the film [the gray band on the left in Fig. 2(b)]. This balance is given by the capillary number Ca $\equiv \mu\dot{\gamma}R/\sigma$. Schwartz and Princen [47] worked out the details and found a sublinear dependence of the shear stress on the rate of strain,

$$\tau \sim \left(\frac{\sigma}{R}\right)\text{Ca}^{2/3}, \tag{8}$$

which was a great achievement because it provided a mechanism for explaining thixotropy (shear thinning). Subsequently Princen and Kiss [27] overcame some of the experimental difficulties associated with shear stress measurements and used a Couette geometry to measure a series of eight oil-in-water emulsions with a range of continuous fractions, $0.024 \le \epsilon \le 0.17$. They adapted a semiempirical model loosely based on the film-stretching model [Eq. (8)] by including a yield stress and reducing the exponent by 25%,

$$\tau=\tau_y+\left(\frac{\sigma}{R}\right)k_P\mathrm{Ca}^{1/2}$$

with

$$\tau_y=\left(\frac{\sigma}{R}\right)[c_1+c_2\log_{10}(\epsilon)](1-\epsilon)^{1/3}$$

and

$$k_P=c_3(\epsilon_c-\epsilon), \tag{9}$$

where $\epsilon_c=0.27$ and the empirical parameters are $c_1=-0.080$, $c_2=-0.114$, and $c_3=32$. Until recent publications by Denkov and co-workers [30,43] and Soller and Koehler [39], Eq. (9) was the only constitutive relation for continuous shearing that accounts for ϵ.

However almost every aspect of Eq. (9) has been called into question by rheological studies from other groups. For example, experiments by Saint-Jalmes and Durian [17] found that foams lose their rigidity at $\epsilon_c=0.36$, which is 30% higher than reported by Princen and Kiss. Measurements using a parallel-plate geometry by Denkov [29] showed that the type of surfactant is an important material parameter; exchanging the surfactant can result in a factor of 2 change in the power-law index (i.e., $n=0.24\rightarrow0.42$). More recently, we performed measurements on a monodisperse soap foam and found that Princen's parameters overpredicted the shear stresses by about a factor of 2 [39].

Coussot *et al.* [48,49] used pastes as a model system for their study of shear-thinning yield-stress fluids, from which they developed a different picture for the yielding transition from elastic deformation to viscoplastic flow. They found that for continuous steady-state shearing there are a minimum shear stress and associated minimum shear rate; for lower stresses the shearing rate fluctuates and is unsteady. They modified a simple power-law relation between the shear stress and rate of strain by imposing a flow rule for the minimum shear rate, $\dot{\gamma}_c$, and critical stress, τ_c, for continuous steady-state shearing,

$$\frac{\tau}{\tau_c}=\left(\frac{\dot{\gamma}}{\dot{\gamma}_c}\right)^n \quad \text{for} \quad \tau\geq\tau_c \quad \text{and} \quad \dot{\gamma}\geq\dot{\gamma}_c. \tag{10}$$

Model of Coussot *et al.* can be rewritten as a Herschel-Bulkley equation by defining the consistency $k_C=(\tau_cR/\sigma)(\sigma/\mu R\dot{\gamma}_c)^n$, setting the yield stress to zero and imposing a threshold stress condition

$$\tau=\left(\frac{\sigma}{R}\right)k_C\mathrm{Ca}^n \quad \text{with} \quad \tau\geq\tau_c. \tag{11}$$

Rodts *et al.* [40] performed wide-gap Couette experiments on a shaving cream foam with MRI imaging to determine the shearing velocity profiles. In agreement with their earlier work on pastes, they observed a shear band that grows in width from the inner rotating cylinder with increasing torque. In that study $\epsilon=0.07$, $R=10$ μm and from their data we extract the power relation $\tau\approx0.07(\sigma/R)\mathrm{Ca}^{0.25}$ for higher shear rates, $\dot{\gamma}\gtrsim1$ rad/s.

An alternative to the film-stretching dissipative mechanism of Princen and Kiss is film shearing [15,30,39,50]. The films are not considered as thin membranes that have plug-like flow as in the Princen model, rather the shearing of the bubbles causes a lubrication flow and the films have a finite (and in some cases even substantial) thickness. Dilatational viscosity of the interfaces, as well as Marangoni forces, results in surface stresses that are directed as indicated by the curved arrows in Fig. 2(c). On a conceptual level, the foam resembles a collection of balloons that are pressed together in a water bath and sheared. Similar to dense granular flows, the bubbles cannot rotate in a coordinated fashion and instead rotational frustration occurs whereby adjacent bubbles and their interfaces rotate in opposing directions. The resulting lubrication flow between the bubbles is shown in Fig. 2(d). Thus the macroscopic shear rate, $\dot{\gamma}$, is locally magnified to $\sim(R/h)\dot{\gamma}$ from which a constitutive relation follows:

$$\tau\propto\frac{\mu R}{h}\dot{\gamma}. \tag{12}$$

If the interfaces remain rigid and the film thickness remains constant this model predicts a linear relationship between stress and rate of strain, which is the main shortcoming of the film-shearing model in its original form, because real foams are shear thinning. However if the film thickness varies with shear rate, $\dot{\gamma}$, or liquid fraction, ϵ, some of the interesting nonlinear rheological behaviors of foams can be accounted for [30,39].

The version of the recent film-shearing model by Denkov *et al.* [30] is based on a film thickness that varies with shear rate and the assumption that Marangoni forces lead to quasirigid interfaces. When opposing bubbles first come into contact a new film is formed, which initially grows in size as the bubbles slide past each other, then shrinks, and finally disappears when the bubbles lose contact. The model assumes monodisperse bubbles arranged in an fcc lattice that have coordinated shear planes. It takes into account the duration, alignment, and geometry of the sheared films. The rate at which newly formed films thin increases with osmotic pressure, which is proportional to the deformation of the bubbles and therefore increases with diminishing liquid content. It disregards the disjoining forces acting on opposing sides of the films; thus it is valid only for cases where the films are sufficiently thick, $h\gtrsim10$ nm, and their thickness is set by shearing. Therefore the model is only valid for larger shear rates and foams whose liquid content is moderate, $0.03\lesssim\epsilon\lesssim0.15$. The predicted shear stress combines an elastic and a viscous component,

$$\tau=\tau_y(\epsilon)+0.806\left(\frac{\sigma}{R}\right)\mathrm{Ca}^{1/2}(1-\epsilon)^{5/6}\epsilon^{-1/2}. \tag{13}$$

Thus Denkov's analysis offers a theory for the shear-thinning behavior, $\tau\sim\mathrm{Ca}^{1/2}$ as observed by Princen and Kiss [27], without adjustable parameters. Because no precise prediction for the elastic contribution to the yield stress currently exists, $\tau_y(\epsilon)$ needs to be measured directly or determined from semiempirical models such as Eq. (9). Note that the restricted range of liquid fraction removes the divergence due to $\epsilon^{-1/2}$ for $\epsilon\rightarrow0$ as well as avoids the rigidity-loss transition

TABLE I. Main features and differences of the three rheological models.

	Princen and Kiss Ref. [27]	Denkov *et al.* Ref. [30]	Soller and Koehler Ref. [39]
Dissipative region	Transitional region	Film	Film
Main source of dissipation	Dilative and contractive	Lubrication	Lubrication
Type of flow in films	Pluglike	Transverse shear	Transverse shear with in-plane swirling
Film thickness	Fixed	Increases with shear rate and liquid content	Increases with liquid content
Elastic yield-stress component	Yes	Yes	No (i.e., $\tau_y=0$)
Valid range of ϵ	Not specified	$0.02 \lesssim \epsilon \lesssim 0.15$	$\epsilon \lesssim 0.2$

for $\epsilon \to \epsilon_c$ where the foam transitions to an easily sheared bubbly fluid.

We recently developed a film-shearing model [39], that is based on observations by Carrier *et al.* [51] showing the film's thickness increases with liquid content. The mechanism for this film swelling remains poorly understood and may be due to drainage flow from the channel-like network leaking into films or Marangoni forces creating a circulatory flow in the films. Accordingly, we write the relationship as

$$h \approx h_0(1 + h'\epsilon), \tag{14}$$

where observations show that the film-swelling parameter, h', diminishes with increasing bubble size. Since the friction between shearing bubbles diminishes proportional to the lubricating film width, it follows $\tau \propto (1+h'\epsilon)^{-1}$. We used the film-thickness dependence for the consistency in the power-law model [Eq. (11)] and proposed

$$\tau = \left(\frac{\sigma}{R}\right)\left(\frac{g}{1+h'\epsilon}\right), \tag{15}$$

where the dimensionless consistency, g, depends on the shear rate. For a soap foam with $R=0.5$ mm bubbles, the measurements indicated a simple power-law dependence $g \approx 2\mathrm{Ca}^{0.2}$, and the film-swelling parameter had a weak logarithmic dependence on shear rate, $h'(\mathrm{Ca}) \approx 10-2\log(\mathrm{Ca})$. Our minimalist model did not include a yielding criterion nor did it account for the rigidity-loss transition at ϵ_c because the fit was sufficiently good not to warrant additional terms and parameters.

Table I outlines the important features, which differentiate the three rheological models. Denkov's model shares similarities with the Princen and Soller models. The dissipative term of the shear stresses is proportional to $\dot{\gamma}^{1/2}$, as is the case for Princen's model. The source of dissipation is lubrication flow in the films, thereby resembling our model. Since our model was developed from FDR experiments, it is primarily based on the dependence of shear stress on liquid volume fraction, whereas the other two models are primarily based on standard rheograms (where the dependence of the shear stress on shear rate is measured).

II. METHODS

The FDR technique is based on creating a steady-state volume of foam in the shearing region, where both liquid volume fraction and bubble size are controlled. The setup is photographed in Fig. 3(a), whose centerpiece is an advanced stress-controlled rheometer (AR2000 by TA instruments). The foam is inside a custom-built cylindrical shear cell and is continuously generated from a foamate reservoir located at the bottom through which N_2 gas bubbles are slowly blown out of glass frit, which is shown schematically in Fig. 3(b). The gas flow rate is controlled by a self-regulating flow valve. The slow regeneration causes the foam to rise at a slow rate, $u_{\mathrm{bubble}}=-0.01$ cm/s. (We choose the z axis to point downward, thus the rising bubbles have negative velocity.) A hot wire loop at the top of the shear cell ruptures the foam emerging from the tube and sets the total height of the foam, $H=20$ cm. The outer cylinder of the shear cell is a 25-cm-long Plexiglas tube with diameter $D_2=3.5$ cm, and to minimize wall slip the inner surface has been roughened. The inner cylinder rotates at angular velocity ω, has diameter $D_1=1.3$ cm, and is covered by rough grit 40 sandpaper to also prevent wall slip. The syringe pump on the left side of the picture perfuses the foam from four needles, which are symmetrically spaced 1 cm from the top of the cell in order to create a uniform perfusion. The syringe pump on the right of the picture withdraws fluid from the liquid reservoir to

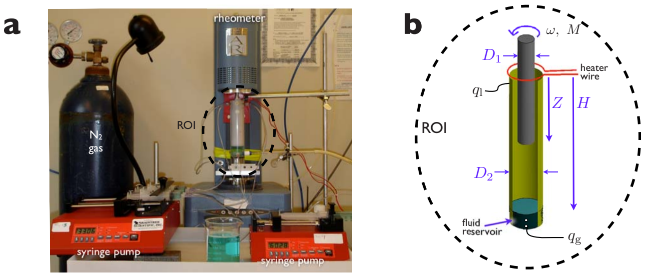

FIG. 3. (Color online) (a) Photograph of the FDR setup, where the two syringe pumps, the N_2 gas cylinder and rheometer are labeled. The dashed ROI is shown schematically in (b). The sample chamber is composed of an outer cylinder, with diameter $D_2=2.35$ cm and height of 25 cm, where the foamate reservoir is contained in the bottom 5 cm, and an inner cylinder, with height $Z=10$ and diameter $D_1=1.3$ cm, which rotates at angular velocity ω. A hot wire at the top pops bubbles and maintains the foam height $H=20$ cm. Fluid is injected at total flow rate q_l, and gas is injected through glass frits inside the foamate reservoir at flow rate $q_g=5$ SCCM (SCCM denotes cubic centimeter per minute at STP), which produces monodisperse bubbles.

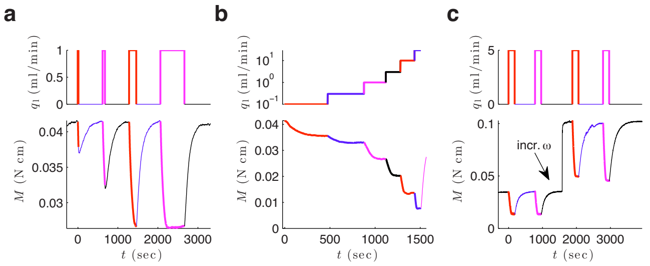

FIG. 4. (Color online) Three types of FDR experiments of the coarse foam. (a) Top: perfusion pulses with $q_l = 1$ ml/min and increasing durations, $T_p = 19, 61, 181, 600$ s. Bottom: torque on rotating inner cylinder, which changes in response to perfusion. (b) Incremental perfusions of increasing flow rates, $q_l = 0.1, 0.3, 1, 3, 10, 30$ ml/min followed by 1 min of no perfusion. In (a) and (b) the angular velocity was fixed, $\omega = 1$ rad/s. (c) Two pairs of $q_l = 5$ ml/min pulses with duration $\Delta T_p = 181$ s, which are separated by 3 min. The angular velocity was increased from $\omega = 0.3$ rad/s for the first pair of pulses to $\omega = 30$ rad/s for the second pair of pulses at $t = 1580$ s and was indicated by the arrow.

compensate for the draining fluid in order to maintain the reservoir fluid height at 5 cm.

A small patch of the outer cylinder was left smooth to allow for visual inspection of the bubbles and their shear. We observed that bubbles moved along the outer wall only for higher angular velocities, $\omega \gtrsim 50$ rad/s. Additionally, higher shear rates changed the quality of the foam by splitting larger bubbles and creating a finer foam.

We used Dawn dish detergent, with concentration of 1% by volume in water, which produces stable bubbles that do not burst. The foamate's surface tension was $\sigma = 20$ dyn/cm. In this study, N_2 gas and two types of fritted glass tubes were used: extra coarse and coarse. Pictures of the bubbles rising inside the fluid reservoir show that they have radii $R = 0.5 \pm 0.2$ mm and $R = 0.2 \pm 0.1$ mm, respectively.

In the FDR experiments fluid perfusion and rotational velocity of the inner cylinder were controlled while the torque due to foam shearing was monitored at a sample rate of ~ 3 Hz. The average shear stress at the inner cylinder's surface is calculated from division of the torque by the surface area of the cylinder, which is

$$\langle \tau \rangle = \frac{M}{\pi D Z}. \tag{16}$$

We have neglected the contribution of the disk at the bottom of the inner cylinder, which results in small overestimates of the average shear stress for uniform foam that are no greater than 3%. Two perfusion sequences were used, which were pulsed perfusion and incremental perfusions where the injection rate increases stepwise. Examples of these sequences are shown in top portions of Figs. 4(a) and 4(b), respectively. The bottom portions show the concomitant changes in the torque on the rotating inner cylinder. Figure 4(c) shows repeated pulsed perfusions with a hundredfold increase in the angular velocity, from $\omega = 0.3$ to $\omega = 30$, which results in threefold increase in torque. All the experiments are variants of these two types of perfusion sequences and the angular velocity is either held constant or changed in steps.

III. RESULTS AND DISCUSSION

We begin with the response of the shear stress due to liquid perfusion in Sec. III A. With no theory and a minimum of assumptions we estimate the drainage rates from the rheological data and make comparisons with foam drainage theory. In Sec. III B we explore the inverse relationship between the average shear stress and the average liquid volume fraction; it is precisely this relationship that is at the heart of our rheological model [Eq. (15)]. Section III C is devoted to modeling incremental perfusion sequences for the coarse and fine foams and performing a self-consistency check with foam drainage theory. This is followed by a section on the shear-rate dependence of the dimensionless consistency of our model, g in Eq. (15), which suggests a hybrid model that combines a film-swelling dependence on ϵ with a Herschel-Bulkley dependence on $\dot{\gamma}$. Finally, in Sec. III E we analyze the effects of changing the shear rate on shear stress for pulsed perfusions in terms of the Herschel-Bulkley, Coussot, and our recently developed hybrid models.

A. Self-similar nature of perfusions

Systematic perfusion procedures result in characteristic changes in the shear stress, which in turn are due to the self-similar nature of foam drainage [52]. This is evident from the infusion pulses of increasing duration resulting in stress drops, as shown in the top and bottom portions of Fig. 4(a). The stress drops are self-similar, which level off for times exceeding 2 min, and all collapse onto a master curve in Fig. 5(a). Likewise, incremental perfusions result in stress drops that have a similar shape although the stresses in successive steps do not collapse in the same fashion as for the pulsed perfusions [compare Figs. 4(a) and 4(b)]. The stresses drop off more rapidly for successively increasing perfusion rates and level off at lower values. The self-similar nature of the normalized stress drops is manifested by their collapse onto a master curve [Fig. 5(c)], where for each incremental perfusion step the time is rescaled by the characteristic drainage time, T_d, over which the normalized stress has dropped by 90%. Moreover, this characteristic time provides an estimate of the drainage velocity because the stresses level off once the foam is uniformly perfused from the point of injection down to the bottom of the rotating inner cylinder, which means the perfusion has reached a distance of $\approx Z$. Accordingly, an estimate for the drainage velocity is

$$u_{\text{est.}} = Z/T_d. \tag{17}$$

The liquid fraction can be estimated from the ratio of the liquid uniformly perfusing the foam to its volume inside the shearing gap,

$$\epsilon_{\text{est.}} = \frac{q T_d}{(\pi/4)(D_2^2 - D_1^2) Z}. \tag{18}$$

Figure 5(d) is a log-log plot of the estimated drainage velocity, obtained from Eq. (17), and the liquid fraction, obtained

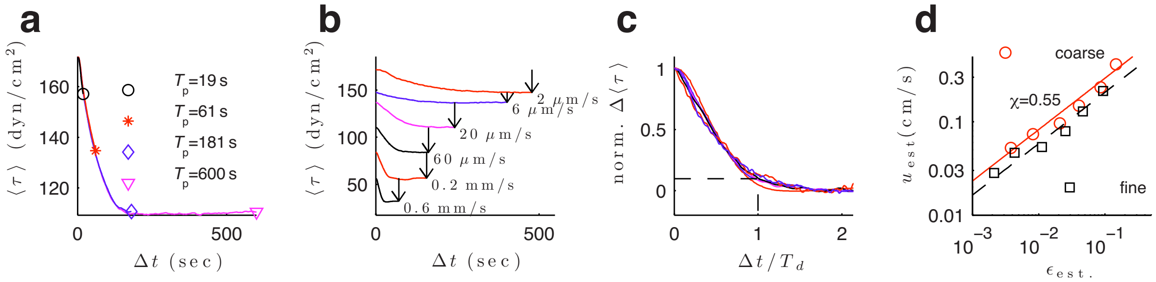

FIG. 5. (Color online) Drops in the shear stress due to fluid perfusion for the coarse foam. (a) The response of the shear stress due to perfusion by four pulses of increasing duration, from Fig. 4(a) collapses. (b) The evolution of the stress drops from the six-step incremental perfusion procedure from Fig. 4(b). (c) Collapse of the normalized stress drops from the incremental perfusion procedure where the time is rescaled by the characteristic drainage time T_d, which corresponds to a 90% drop. (d) The drainage velocity obtained from Eq. (17) versus the liquid fraction obtained from Eq. (18). The solid and dashed lines are the best fits to the mobile interface drainage model with χ=0.55 for the coarse and fine foams, respectively.

from Eq. (18), for both the coarse and fine foam. Thus the FDR experiment can be used to detect extremely low drainage rates because the rheometer is very sensitive to small changes in torque, which result from small changes in the foam's liquid volume fraction. Moreover, it is possible to estimate the drainage rate based only on two rudimentary assumptions: (i) long perfusions result in a uniform liquid volume fraction and (ii) shear stresses monotonically diminish with increasing liquid volume fraction.

We next compare the u dependence on ϵ with an earlier study using the same soap [5]. As summarized in Appendix A, the permeability exponent was found to be $\chi \approx 0.55$, which we use for the logarithmic slopes in Fig. 5(d). The velocity prefactors from the fits are given in the third column of Table II, which according to Eq. (2) is KL^2/μ (note that the capillary term can be dropped for determining the average velocity). Using the channel length estimated from the bubble radius, $L=0.718R$, we report the permeability prefactor estimated from the data in the fourth column of the Table II. In the case of the coarse foam this estimate agrees well with the value obtained by interpolating data from previous work given in the last column. For the fine foam however the estimated permeability prefactor is almost double that based on the extrapolation from previous work, which means that the fine foam drains almost twice as fast as one would expect from the three bubble sizes analyzed in an earlier letter [5]. Possible causes for this discrepancy are as follows. (1) The fine foam coarsens about twice as rapidly as the coarse foam, thus the average bubble size will have grown in the half hour it takes to move into the shearing gap, which in turn leads to a faster drainage rate. (2) The theoretical velocity is based on an entirely empirical extrapolation of the permeability prefactor to our much finer foam (the finest foam in previous work had $R=0.7$ mm that is several times larger), which has no theoretical basis. (3) The finer foam has far greater measurement noise, which contributes to the errors of determining the characteristic drainage time.

TABLE II. Velocity and permeability prefactors determined from the self-similar analysis.

	R (cm)	$K\rho g L^2/\mu$	Estimated K	K from Eq. (A1)
Coarse	0.05 ± 0.01	1.04 ± 0.17	0.0082 ± 0.0014	0.0092
Fine	0.02 ± 0.01	0.73 ± 0.08	0.0362 ± 0.0042	0.018

B. Effects of the changing liquid fraction on rheology

Having established that foams in the FDR setup drain as expected, albeit in the case of the fine foam the permeability prefactor is somewhat greater than naive extrapolation from earlier work predicts; we include foam drainage simulations for a more quantitative analysis involving $\epsilon(z,t)$ based on Eq. (6). The permeability parameters are given in Appendix A; K decreases with bubble size as described by Eq. (A1) and χ=0.55. The calculations were performed using MATLAB and details are given in Appendix B.

Figure 6(a) is a spatiotemporal plot of the liquid volume fraction evolving as four pulses of increasing duration are injected; the perfusion sequence is given in Fig. 4(a). The brightness is proportional to the liquid fraction and the width of the bright bands is given by the perfusion time. Similar to the average shear stress [Eq. (16)], we define the average liquid volume fraction of the foam in the gap surrounding the rotating inner cylinder,

$$\langle\epsilon\rangle = \int_{z<Z} \epsilon(z,t)\left(\frac{dz}{Z}\right), \tag{19}$$

which is shown in Fig. 6(b). Note the inverse relationship between the modeled mean liquid fraction about the inner cylinder and the measured mean shear stress on the inner cylinder in Fig. 4(a). When $\langle\epsilon\rangle$ reaches an upper plateau, $\langle\tau\rangle$ descends to a local minimum and vice versa. Thus, it is natural to consider the inverse relationship τ^{-1} vs ϵ, which is shown in Fig. 6(c) for all three experiments from Fig. 4. The correlation is linear, thereby implying $\tau=g/(1+h'\epsilon)$, which is the foundation of the Soller-Koehler model [39]. The slight amount of hysteresis is to be expected because changes in the perfusion cause spatial variations in ϵ and τ and the local relationship does extend to a global average, i.e., $\langle\tau\rangle \neq g/(1+h'\langle\epsilon\rangle)$.

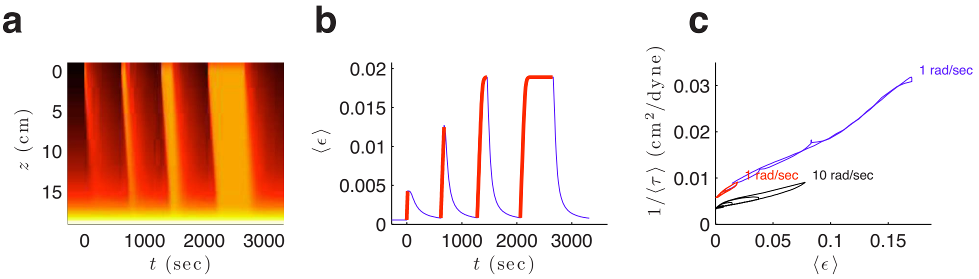

FIG. 6. (Color online) Evolution of the liquid volume fraction and shear stresses for the coarse foam. (a) Spatiotemporal plot of the calculated liquid volume fraction for the four perfusion pulses of increasing duration shown in Fig. 4. The brightness indicates liquid content, and at the bottom of the foam $\epsilon=\epsilon_c$. (b) Evolution of the average liquid volume fraction of the foam surrounding the inner rotating cylinder [see Eq. (19)]. (c) Correlation between the average inverse shear stress and the average liquid volume fraction for three experiments. These include the four pulses from (b), shown in red (bright gray), and the six-step incremental perfusion, shown in blue (dark gray), from Figs. 4(a) and 4(b), respectively, which are both for $\omega=1$ rad/s. Also included is a four-step, $q_l=9$ ml/min, pulsed perfusion performed at $\omega=10$ rad/s, shown in black.

C. Modeling incremental perfusions at fixed shear rate

We calculate the evolving liquid volume fraction for incremental perfusions in order to evaluate the models by Princen and Soller. We do not separately treat the model by Denkov *et al.* because it gives values very close to those of Princen albeit its formulation is more complex and based on a rigorous analysis. Since Coussot's model does not have an ϵ dependence, it is not applicable for incremental perfusion experiments. We then optimize the parameters of the remaining two models for both foams in terms of the best experimental fit and find for the Princen model that emulsion parameters differ substantially from those of foams. We conclude this section with a self-consistency analysis of the Soller model.

In order to quantify the fitting quality, we use the mean relative variance between the measured and modeled shear stresses,

$$\mathcal{E}=\sum_{i=1}^{N}\left(\frac{\tau_{\text{measurement},i}}{\tau_{\text{fit},i}}-1\right)^2/N, \tag{20}$$

for a data set of $i=1,2,\ldots,N$ measurements. Since the experiments lasted for several minutes and data were acquired at 3 Hz, the number of measurements typically was $N\sim10^3-10^4$.

The thick gray curves in Fig. 7 show incremental perfusion FDR experiments for both the fine and coarse foams. The dashed blue (dark gray) lines show predictions from Princen's model using original parameters, which were derived from emulsion experiments. For the fine foam the shear stresses are overestimated by about 50%, whereas for the coarse foam the shear stresses are underestimated by about 20%. We optimize Princen's parameters to our foam experiments by minimizing $\mathcal{E}$, shown as dotted-dashed curves, and report them in Table III. The fitting errors using emulsion parameters are $\mathcal{E}=0.05,0.03$ for the fine and coarse foams, respectively, which are reduced more than tenfold upon optimization—see the fifth column of Table III. Optimization has changed the yield-stress parameters, c_1, c_2, which reduced the yield stress and consequently the strain-dependent prefactor, c_3, has increased.

Finally, the solid black line shows the optimized fits using the Soller model, which in the case of the coarse foam are in agreement with our previous publication [39] (the fine foam was not included in this earlier work). As is evident from the table, the Soller model achieves a smaller fitting error $\mathcal{E}$ although it has one less free parameter than Princen's three-parameter model.

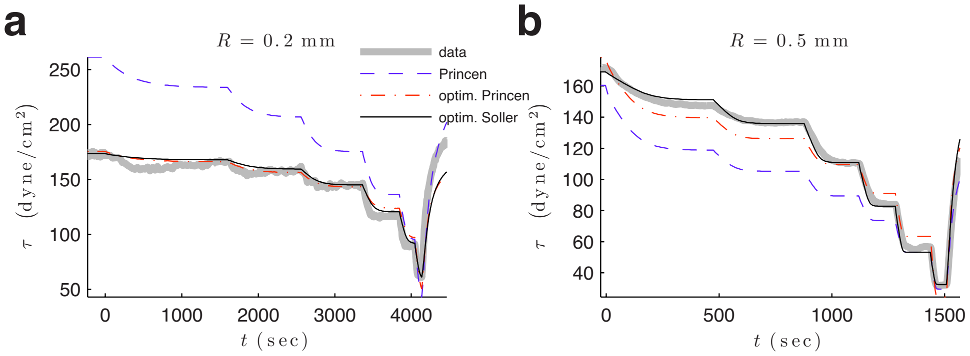

FIG. 7. (Color online) Applying Princen's film-stretching model [27] and Soller's film-shearing model [39] to the incremental perfusions with the inner cylinder rotating at $\omega=1$ rad/s. The wide gray curve shows the data; the dashed blue (dark gray) lines show Princen's model using emulsion-derived parameters. The continuous black curve shows the optimized Soller model and the dotted-dashed red (light gray) curve shows Princen's model using optimized parameters, which are given in Table III.

TABLE III. Parameters for the incremental perfusions shown in Fig. 7. The first row shows Princen's published values for emulsions. Uncertainties based on 95% confidence intervals are supplied where appropriate.

	Princen [Eq. (9)]				Soller [Eq. (14)]		
	c_1	c_2	c_3	$\mathcal{E}$	g	h'	$\mathcal{E}$
Emulsion	−0.08	−0.114	32				
$R=0.2$ mm	-0.053 ± 0.013	-0.034 ± 0.005	66 ± 10	7×10^{-3}	0.182 ± 0.002	11.3 ± 0.6	5×10^{-3}
$R=0.5$ mm	-0.198 ± 0.017	-0.104 ± 0.004	86 ± 7	1×10^{-2}	0.430 ± 0.002	28.4 ± 0.6	3×10^{-3}

We next check the Soller film-shearing model for self-consistency by simultaneously optimizing *all* parameters, which are three foam drainage parameters from Eq. (6), R, χ, and K, as well as the two shearing parameters from Eq. (15), g and h'. If this model is self-consistent, then the optimized values for K and χ should conform to expectations based on foam drainage theory, and the optimized bubble size should agree with estimates obtained from images. Moreover the optimized shearing parameters, g and h', for the coarse and fine foams should be consistent with those from previous work [39] and in agreement with those of Table III above. Conversely, doubt is cast upon the Soller model if the optimized parameters are inconsistent with expectations.

We perform simulations of the liquid volume fraction for sets of drainage parameters that span the parameter space $R\times\chi\times K$ and determine the best shearing parameters, g and h', for fitting the data. We identify the optimum parameter set (R,χ,K,g,h'), which has the smallest fitting error $\mathcal{E}$, for self-consistency comparisons. Figures 8(a)–8(c) show the variations in $\mathcal{E}$ for the three drainage parameters about their optimized values, which are listed in Table IV. The associated uncertainty intervals were determined such that 68% of the data points are contained within the corresponding band of values calculated by the model. For the coarse foam the literature values lie within uncertainty estimates of the optimized values:

(1) The optimized bubble size agrees with visual observations when considering the degree of measured polydispersity is ~30%.

(2) Within error estimates the optimized permeability exponent, χ, agrees with previous work summarized in Appendix A.

(3) The optimized permeability prefactor, K, agrees well with that calculated from the bubble size [using $R=0.5$ mm in Eq. (A1)].

We next discuss the fine foam. We find the same difficulty as observed for the self-similar analysis of the incremental perfusion experiment in Sec. III A, which is that the fine foam drains faster than expected based on extending previous work. In summary we find the following:

(1) The optimized bubble size is somewhat greater than expected but still contained within the degree of polydispersity. The bubble size was measured at the bottom of the foam column, and during 20 min for the bubbles to migrate into the region surrounding the inner cylinder they will be somewhat larger due to coarsening.

(2) The permeability exponent is in accord with previous work.

(3) The permeability prefactor is about twice that expected from extrapolating the data of previous work, where the bubbles were 6–20 times larger. However there is no theory for the dependence of the permeability prefactor on the bubble size, and therefore this discrepancy may be due to the *ad hoc* nature of extrapolation over such a large range. Moreover, a similar large value for the permeability prefactor was also observed in the self-similar analysis of Sec. III A above.

The shearing parameters, g and h', are comparable to those obtained previously using *different* drainage parameters (compare Tables III and IV), but the fitting errors have been reduced fivefold. In particular, had we included the optimized fit in Fig. 7(a); it would have lain on top of the data (but to avoid cluttering it was not plotted). Thus the analysis of both foams shows self-consistency; however, our rheological measurements indicate that the fine foam drains faster than expected based on a naive extrapolation of previous data, which has also been noted by Carrier *et al.* [51].

D. Constitutive relation

Historically, research has focused on determining constitutive equations, which relate the stress to the shear rate

TABLE IV. Comparing the optimized foam drainage parameters with values expected from previous work [see Appendix A and Eq. (A1) for K]. The last three columns give the shearing parameters and fitting error.

		R (cm)	χ	K	g	h'	$\mathcal{E}$
Fine foam	Optimized	0.025 ± 0.002	0.6 ± 0.04	0.027 ± 0.009	0.23 ± 0.001	21 ± 0.5	9×10^{-4}
	Expected	0.02	0.55	0.0139			
Coarse foam	Optimized	0.043 ± 0.002	0.55 ± 0.04	0.0072 ± 0.003	0.37 ± 0.001	22 ± 0.2	8×10^{-4}
	Expected	0.05	0.55	0.00733	0.42 ± 0.002 [a]	30 ± 4 [a]	

[a] Values taken from [39].

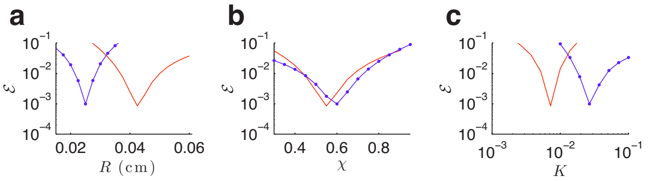

FIG. 8. (Color online) Error analysis of the drainage parameters for the coarse and fine foams using $\omega=1$ rad/s incremental perfusion sequences, shown as solid red (light gray) and dotted blue (dark gray) curves, respectively. The optimum parameter values are given in Table IV.

while attempting to keep the liquid volume fraction *fixed*. Having established the inverse relationship between liquid fraction and stress at a constant rate of shear in terms of the film-swelling picture, we determine the shear-rate dependence of the shearing parameters, g and h', from Eq. (15) based on the optimized drainage parameters given in Fig. 8 and Table IV. We therefore are implicitly assuming that shearing does not significantly influence drainage, which we confirm subsequently in the Sec. III E. In particular we examine whether the shear-rate dependence of the dimensionless consistency, g, favors the Herschel-Bulkley model with a non-negligible yield stress or the simpler power-law model we proposed earlier [39].

Figure 9(a) shows the dependence of the dimensionless consistency g from Eq. (15) on the dimensionless angular velocity $\mu\omega R/\sigma$ for the coarse foam. We report only intermediate range of angular velocities, $0.02 \leq \omega/(\mathrm{rad/s}) \leq 50$, because for faster rotation larger bubbles are sheared into smaller bubbles and for slower rotation the fluctuations (i.e., noise) in the torque become too large. On the log-log plot g exhibits a mild curvature that is better fit by a power law with an additive constant than a straight line. Thus the shearing prefactor shows a Herschel-Bulkley trend, and we formulate a hybrid model by combining the Herschel-Bulkley shear-rate dependence [Eq. (7)] with a film-shearing liquid volume fraction dependence [Eq. (15)],

$$\tau = \left(\frac{\sigma}{R}\right)\left(\frac{g_0 + (\mu\omega R/\sigma)^n g_1}{1 + h'\epsilon}\right), \qquad (21)$$

where g_0, g_1 are the dimensionless yield stress and consistency, respectively. The solid blue (dark gray) curve captures the trend of the measurements much better than the simple power law used in our previous publication [39],

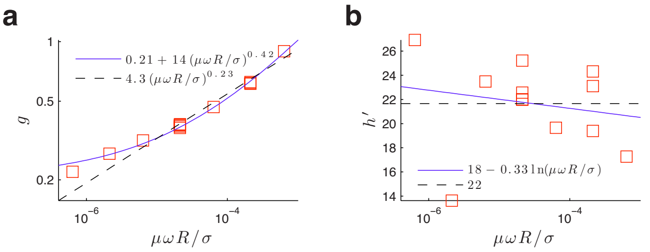

FIG. 9. (Color online) Fitting parameters for the coarse foam. (a) Dependence of the dimensionless consistency, g, on the dimensionless angular velocity, which is fitted by the hybrid model [Eq. (21)], solid blue (dark gray) curve, and the power-law model [Eq. (22)], dashed black line. (b) Dependence of the film-swelling parameter, h', on the dimensionless angular velocity, where the solid blue (dark gray) line shows a logarithmic diminishing trend and the dashed black line shows the average. Fits are given in the legends and for g also in the first row of Table V.

$$\tau = \left(\frac{\sigma}{R}\right)\left(\frac{(\mu\omega R/\sigma)^n g_2}{1 + h'\epsilon}\right), \qquad (22)$$

which is shown as a dashed black line and has a fitting error ten times greater (see Table V). The differences between our current and earlier work are that some new FDR experiments are included, the optimized foam drainage parameters used here are slightly different, and the calculations of the liquid volume fraction are more accurate because foam expansion at high values of ϵ is taken into account—see Eq. (1) in Sec. I A. It is noteworthy that the power-law index for the hybrid model is close to $n=1/2$, which is in agreement with the observations of Princen and Kiss [27] and the calculations by Denkov *et al.* [30].

Figure 10 shows the dependence of g and h' on the dimensionless angular velocity for the fine foam where the fitting parameters are also given in Table V. Repeated measurements show that the scatter of the dimensionless consistency, g, shown in Fig. 10(a), is much larger than for the coarse foam. The data are fit equally well by the Herschel-Bulkley and power-law models: the fitting error for both is the same (cf. the fifth and eighth columns of Table V). Experimental improvements, such as maintaining a more stable foam column height to reduce fluctuations in the torque measurements, are necessary to discriminate between the two models. Similar to the coarse foam, Fig. 10(b) indicates that the film-swelling parameter has a weak logarithmic decreasing trend with angular velocity, which given the large uncertainties can also be effectively approximated as a constant. We note that the values of the averages of the film-swelling

TABLE V. Fits to the dimensionless consistency, g, from Figs. 9(a) and 10(a) for both the hybrid and power-law models. The uncertainties were calculated using 95% confidence intervals.

	Hybrid model [Eq. (21)]				Power-law model [Eq. (22)]		
	g_0	g_1	n	$\mathcal{E}$	g_2	n	$\mathcal{E}$
Coarse	0.21 ± 0.04	14 ± 6.2	0.42 ± 0.06	0.0012	4.3 ± 1.1	0.23 ± 0.03	0.01
Fine	0.11 ± 0.16	11 ± 35	0.4 ± 0.4	0.03	3.3 ± 2	0.25 ± 0.08	0.02

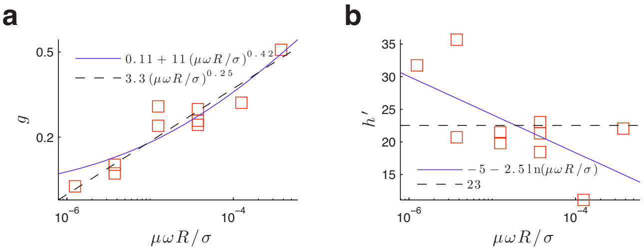

FIG. 10. (Color online) Fitting parameters for the fine foam. Dependence of (a) the dimensionless consistency, g, and (b) the film-swelling parameter, h', on the dimensionless angular velocity. Fits to both models are given in the legends and for g also in the second row of Table V.

parameters for both foams are the same and agree with those obtained in Table IV in Sec. III C.

Figures 9(b) and 10(b) are semilogarithmic plots of the film-swelling parameter, h', versus the dimensionless angular velocity for the coarse and fine foams, respectively. Similar to the dimensionless consistency, the film-swelling parameters for both foams are similar; unfortunately, the scatter is large enough to obscure any clear trends. The solid blue (dark gray) lines show logarithmic fits, whose coefficients are given in the legends. The dashed black lines show the mean values of h', which are almost the same for both foams: 22 ± 2 and 23 ± 5. We note that these values are in agreement with those obtained for the incremental perfusion experiments listed in Table IV in Sec. III C.

E. Pulsed perfusions at different shear rates

Up to this point we have focused on FDR experiments performed at constant shear rate and varying liquid volume fractions. Here we focus on experiments involving the coarse foam where the shear rate also is changed on the fly, as shown in Fig. 4(c) in Sec. II. We use the optimized drainage parameters determined in Sec. III D and show that shearing has a negligible effect on drainage. Based on these measurements we evaluate the effectiveness of the Herschel-Bulkley model [Eq. (9)], as well as Coussot's power-law model [Eq. (10)] and our hybrid model [Eq. (21)]. We finish by comparing the fitting parameters obtained here with those from previous sections.

Figure 11(a) shows the evolution of the shear stresses for a series of five successive identical 3-min-long $q_l = 5$ ml/min perfusions, where the angular velocity increases stepwise roughly by factors of 3 from $\omega = 0.3$ to $\omega = 30$ rad/s. Initially the foam is dry and the shear stresses start at their maximal plateau values. Perfusion results in diminished stresses, which level off at $t \approx 75$ s as indicated by the dashed vertical lines. Figure 11(b) shows that the relative changes in the shear stresses are similar and occur at the same times within a few percent for all five shear rates. Thus we conclude that for moderate rates of shear the drainage process is unaffected; however, at high shear rates, $\omega \gtrsim 50$ rad/s, larger bubbles split into smaller bubbles and thus slow the drainage dynamics. Considering that the applied shear is orthogonal to the drainage flow, the apparent decoupling of shearing and drainage is intuitive, but for the case where the shear and drainage are aligned one might expect some coupling effects.

In our examination of Coussot's model we first demonstrate that the shear band is contained between the cylinders and does not extend to the outer wall. For the sake of argument, we assume that shear stresses throughout the gap exceed the critical stress and therefore the threshold flow condition is superseded by the no-slip boundary condition. Accordingly the shear stress at the inner cylinder, $r = D_1/2$, simplifies to $\tau \propto k_C \omega^n$ [see Eq. (C5) in Appendix C]. Having established that the liquid fraction is unaffected by the shear rate, it follows that the consistency term, k_C, changes the same way for all five trials. Consequently the ratio of the stress with that from a reference trial should remain constant, i.e., $\langle\tau\rangle / \langle\tau_{\mathrm{ref}}\rangle = (\omega/\omega_{\mathrm{ref}})^n$. But Fig. 11(c) shows that the ratio increases by as much as 25% during perfusion, thereby indicating for Eq. (10) to hold that the critical stress is sufficiently large to be relevant for our experiments and that instead the shear band has to be growing radially with increasing angular velocity. For example, the 25% increase during perfusion could result from a decrease in the critical stress with increasing ϵ that results in the shear band shrinking for slower rotation, whereas for faster rotation the shear band still extends across the gap. Therefore in order for Coussot's model to hold, the relationship between the angular velocity and shear stress for localized shear banding applies,

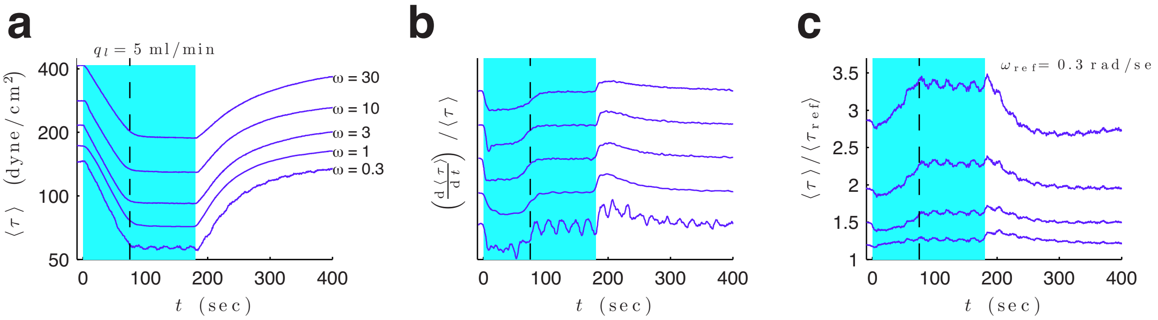

FIG. 11. (Color online) Pulsed perfusion experiments of 3 min duration, indicated by the cyan (light gray) background, which are repeated at five shear rates for the coarse foam. The dashed black lines at $t = 75$ s show the onset of saturation at the lower shear stress. (a) The evolution of the mean shear stress for five angular velocities, $\omega = 0.3, 1, 3, 10, 30$ rad/s. (b) The relative changes in shear stress are offset in the plot to compare the drainage dynamics. (c) The evolution of the mean shear stress relative to that for $\omega_{\mathrm{ref}} = 0.3$ rad/s.

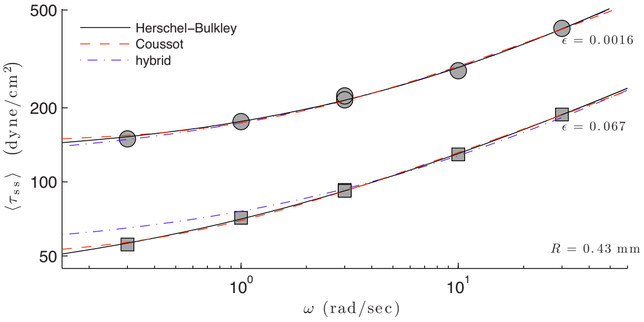

FIG. 12. (Color online) The dependence of the steady-state shear stresses on angular velocity for the uniformly dry, ϵ=0.0015, and wet, ϵ=0.066, portions of the pulsed perfusion experiments. Three types of fits are included and their fitting values are given in Table VI below. The liquid fractions have been calculated using optimized foam drainage parameters given in Fig. 8.

$$\frac{\tau}{\tau_c} = \left[\left(\frac{2\mu R \omega}{n\sigma} \right) \left(\frac{\sigma k_C}{R \tau_c} \right)^{1/n} + 1 \right]^n, \tag{23}$$

which follows directly from Eq. (C5) in Appendix C. (Below we verify the self-consistency of this assertion by showing that indeed the critical stress is non-negligible.)

A more quantitative assessment of the threshold and yield stress can be achieved by considering the steady-state shear stresses of the pulsed perfusion experiments. These are the lower shear stress plateaus where the perfusion has produced a uniformly wet foam and the upper shear stresses where the foam is drained. Figure 12 shows the relationship between steady-state shear stresses and angular velocities have a curvature similar to that in Fig. 9(a), which again indicates that our simple power-law dependence [39] is inadequate. Included are fits to the Herschel-Bulkley and Coussot models for the wet and dry regimes separately and their fitting parameters are given in Table VI. The threshold stresses and consistencies for both models diminish with increasing ϵ and are remarkably similar, and only the power-law indices are noticeably different: for Herschel-Bulkley $n \approx 1/2$ whereas for Coussot $n \approx 1/3$. Recall that Coussot's shaving cream experiments [40] indicate that the power-law exponent is $n \approx 1/4$. The fitting errors for the Herschel-Bulkley model are smaller. Additionally, the larger range of confidence intervals for the Herschel-Bulkley model indicates its formulation is more amenable to the data.

We now verify the self-consistency of our assumption and visual observations that the shear band is contained within the gap and for moderate rates of shear does not extend to the outer cylinder. The greatest shear stresses in Fig. 12 are $\tau_{\max}$=190 and 420 dyn/cm^2 for the wet and dry regimes. Since the shear stresses diminish radially with r^{-2}, they drop to 57 and 129 dyn/cm^2 at the outer wall. These wall stresses are comparable to the threshold stresses in the table, which shows that for our range of experiments the shear band is contained within the gap and only spreads to the outer cylinder at the highest rates of shear. Thus our assumption for using Eq. (23) is justified.

The values of the two steady-state liquid volume fractions, ϵ=0.0015, 0.066, give two sets of predictions for the consistency and yield stress using Princen's model, τ_y =90, 264 dyn/cm^2 and k_P=9.4, 11. As we observed previously [see Fig. 7(b)], these predictions are roughly two times too large and are due to extrapolation from emulsion experiments. We also use the liquid volume fractions to fit our hybrid model [Eq. (21)], which is shown as a dotted-dashed blue (dark gray) curve in Fig. 12 as well as the last row in Table VI. Within uncertainties the shearing parameters, g and h', are in agreement with those determined in Sec. III D (cf. Tables V and VI). Rather than six fitting parameters, the hybrid model only requires four, and aside from the lowest shear stress measurement, agreement with the data is better than 10%.

IV. CONCLUSIONS

We have demonstrated the utility of the foam drainage rheology technique for measurement of the stresses occurring in continuously sheared foams where aging effects have been removed. Since all Earth-bound foams drain, incorporating drainage into the rheological procedures is necessary for accurate results. Rather than trying to prevent or minimize drainage during rheological measurements, drainage and perfusion are integral parts of the FDR technique that are used to adjust the liquid volume fraction. Moreover, the foam is continually replenished inside the shear cell, thereby maintaining a steady bubble-size distribution. Thus in a single experiment both the liquid fraction and the shearing rate can easily be varied, which is impossible using conventional batch measurement methods. The FDR technique opens up new avenues for performing controlled rheological experiments providing ramifications for the mechanical behaviors

TABLE VI. Fitting parameters for the pulsed perfusions at different shear rates shown in Fig. 12. The uncertainties are calculated using 95% confidence intervals.

Model	ϵ	Threshold stress ($\frac{\text{dyn}}{\text{cm}^2}$)	Consistency	n		$\mathcal{E}$
Herschel-Bulkley	0.0016	τ_y=125 ± 45	k_{HB}=14 ± 17	0.52 ± 0.19		5×10^{-4}
	0.067	τ_y=35 ± 8	k_{HB}=3.9 ± 1.1	0.43 ± 0.05		7×10^{-5}
Coussot	0.0016	τ_c=145 ± 36	k_C=5.9 ± 5	0.34 ± 0.13		9×10^{-4}
	0.067	τ_c=49 ± 10	k_C=2.5 ± 0.7	0.33 ± 0.04		3×10^{-4}
Hybrid[a]	(All)	$\sigma g_0/R$=121 ± 29	g_1=25 ± 18	0.49 ± 0.11	h'=21 ± 2	3×10^{-3}

[a] The dimensionless yield stress for the hybrid model is g_0=0.30 ± 0.07.

of a wide variety of soft condensed-matter systems. Examples might include stress-strain behavior of biological systems that are perfused with nutrients [53,54], the effects of fluid flow on the shape of plant leaves [55] or fluidized beds whose packing density depends on flow rate [56,57].

We have used the FDR technique to perform a systematic investigation of the rheology of draining coarse and fine foam for a large range of shear rates and liquid volume fractions. With a minimum of assumptions we have verified that slow to moderate shearing has a negligible effect on the dynamics of foam drainage and, we have been able to calculate the liquid volume fraction that results from perfusion. We have compared experimental measurements with three different models, which are a Herschel-Bulkley model, a power-law model with a threshold shear stress, and our power-law model with a liquid volume dependence based on an increasing film thickness with ϵ that is due to drainage. From the analysis of the coarse foam it became evident that our hybrid model, which combines a Herschel-Bulkley dependence of the shear stress on rate of strain with a film-swelling dependence on the liquid volume fraction, is more suitable. However the quality of the data obtained for the fine foam was insufficient to effectively discriminate between the different models, which should be addressed in future studies.

Closely related future work involving the FDR technique includes varying the foam's composition as well as the type of rheological experiments. The sensitivity of modern rheometers also makes the FDR technique ideal for studying foam drainage where other methods are not suitable. Different types of rheological measurements should be performed such as oscillatory shearing and stress/strain relaxation, as well as determination of the yield stress for different liquid volume fractions. It would be interesting to compare rheological experiments performed in microgravity with Earth-bound FDR experiments because in the absence of fluid drainage the film thickness should be decoupled from the liquid volume fraction, and thus we expect the shearing behavior to differ. In particular, we anticipate that models that focus on the film's thickness dependence on shearing, such as that of Denkov *et al.* [30], to be more suitable than our model that focuses on the film's thickness dependence on drainage. Another question that should be addressed is anisotropy: how does the orientation of the shearing plane relative to the direction of the drainage flow affect the shearing stresses and drainage? Given the observations of Carrier and Colin [58] of anisotropic distribution of liquid within a draining foam, we expect that the orientation of the shearing plane likely will affect rheological measurements.

ACKNOWLEDGMENTS

We thank Proctor & Gamble's support of this project and a referee for pointing out that the logarithm in Princen's formula [Eq. (9)] is base 10. Funding by the National Science Foundation Grant No. CTS-0626191215 is acknowledged as is the hospitality of the Aspen Center for Physics.

APPENDIX A: DEPENDENCE OF A FOAM'S PERMEABILITY ON THE BUBBLE SIZE

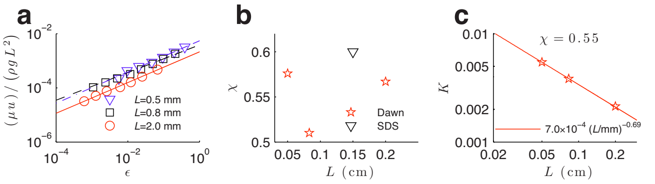

FIG. 13. (Color online) (a) The relationship between the dimensionless drainage velocity, $u/\rho g L^2 \mu$, and the liquid volume fraction for three monodisperse foams made with Dawn having edge lengths $L=2.0, 0.8, 0.5$ mm, taken from [5]. Dependence of the (b) permeability exponents and (c) permeability prefactors on edge length for the three Dawn foams and an SDS foam [59].

We reanalyze drainage experiments published earlier [5] of a foam also made with Dawn dish detergent. We aim to determine how bubble size affects the drainage permeability prefactor, K, and the permeability exponent, χ [cf. Eq. (4)]. Figure 13(a) shows the dependence of the dimensionless drainage velocity on the liquid volume fraction for foams of three bubble sizes, $R=2.7$, 1.1, and 0.7 mm. The data sets evidence power-law behavior of roughly the same exponent, but the three data sets do not fall on top of each other. It follows $(\mu u)/(\rho g L^2)=K\epsilon^{\chi}$, where K *varies* with bubble size. The reasons for the bubble-size dependence remain unclear; possibly films make a significant contribution to the drainage process for smaller bubbles [51]. The interfaces are highly mobile, as evidenced by swirling interference patterns inside the films, and thus it is natural to expect that their permeability exponents approach 1/2, which is confirmed by Fig. 13(b). The permeability exponents are centered about $\chi=0.55$, without any apparent trends with bubble size. However the permeability prefactor, shown in Fig. 13(c), exhibits an increasing trend with decreasing bubble size. For lack of a better understanding, we use the straight line to formulate an entirely empirical power-law relationship,

$$\begin{aligned} K &= (7\pm2)\times10^{-4}\left(\frac{L}{\mathrm{cm}}\right)^{-0.7\pm0.1} \\ &= (9\pm2)\times10^{-4}\left(\frac{R}{\mathrm{cm}}\right)^{-0.7\pm0.1}, \end{aligned} \tag{A1}$$

where the last equality comes from the Kelvin bubble approximation $R=1.39L$.

APPENDIX B: FOAM DRAINAGE SIMULATION DETAILS

The foam drainage simulations were performed using MATLAB's pdepe function, which solves boundary value problems for parabolic-elliptic partial differential equations. Due to the singular nature of the capillary term, $\nabla(\sigma/r)$, in the foam drainage equation that leads to numerical instabilities for dry foams, we choose to simulate the spatiotemporal evolution of the aspect ratio $\kappa=L/r$ instead of r or ϵ. Thus we rewrite Eq. (6) as

$$\begin{aligned} &-\frac{2\delta_c(1-\epsilon)^{2/3}+3\delta_n\kappa^{-1}(1-\epsilon)}{\kappa^3+\frac{2}{3}\delta_c\kappa(1-\epsilon)^{-1/3}+\delta_n}\partial_t\kappa+\frac{KL^2\rho g}{\mu} \\ &\quad\times\nabla\left[\epsilon^{\chi+1}\left(\hat{\mathbf{z}}+\frac{\sigma}{\rho g L}\nabla\kappa\right)-\frac{\psi_{\mathrm{gas}}\mu}{KL^2\rho g}\left(\frac{\epsilon}{1-\epsilon}\right)\hat{\mathbf{z}}\right] \\ &= \psi_l\delta(\mathbf{x}). \end{aligned} \tag{B1}$$

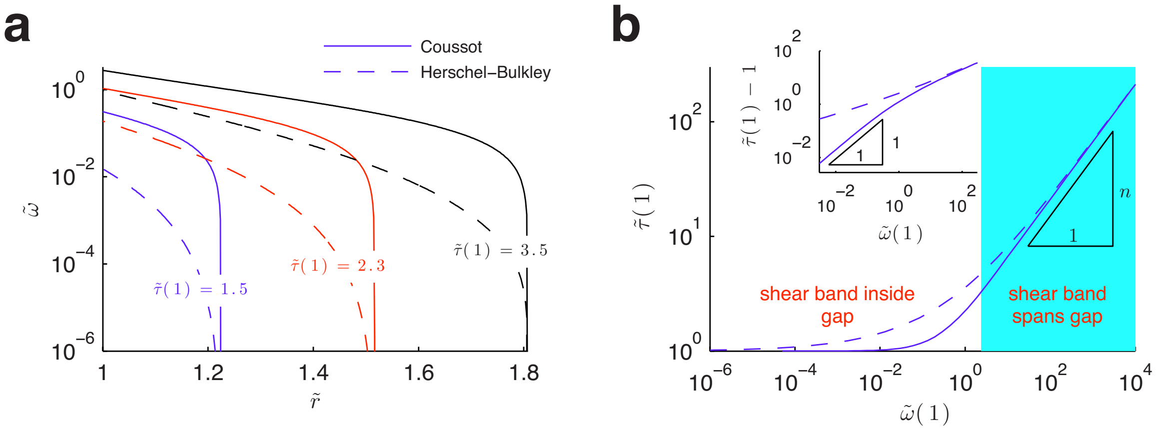

FIG. 14. (Color online) Comparing the Coussot and Herschel-Bulkley models shown as solid and dashed lines, respectively. (a) The radial dependence of the angular velocity for three different applied shear stresses, $\tilde\tau(1)=1.5, 2.3, 3.5$. (b) The relationship between the applied shear stress and the angular velocity at the inner cylinder. The shaded cyan (light gray) region shows the range of angular velocities where the shear band extends across the gap. The inset details how the shear stresses approach unity in the limit of small angular velocity. In the simulations $n=1/2$ and the gap geometry is the same as for the experiments (i.e., $D_2/D_1=1.81$).

To perform the simulations we nondimensionalize using the capillary length and time scale,

$$\ell=\frac{\sigma}{\rho g L} \quad \text{and} \quad t_0=\frac{\mu\sigma}{KL^3(\rho g)^2}. \tag{B2}$$

Nondimensionalized variables are denoted by tilde superscripts, e.g., $\tilde z$, and the foam drainage equation with perfusion and bubbling that is valid at high liquid fraction in one dimension becomes

$$-\frac{2\delta_c(1-\epsilon)^{2/3}+3\delta_n\kappa^{-1}(1-\epsilon)}{\kappa^3+\frac{2}{3}\delta_c\kappa(1-\epsilon)^{-1/3}+\delta_n}\partial_{\tilde t}\kappa + \partial_{\tilde z}\left[\epsilon^{\chi+1}(1+\partial_{\tilde z}\kappa)-\Lambda\left(\frac{\epsilon}{1-\epsilon}\right)\right] = \tilde\psi_l\delta(\tilde z), \tag{B3}$$

where $\Lambda=(\psi_{\text{gas}}\mu)/(KL^2\rho)$ and $\tilde\psi_l=\psi_l t_0/\ell$.

The initial steady state prior to perfusion is when the flux term inside the bracketed term, $[\cdots]$, on the left-hand side of Eq. (B3) is zero, thus the liquid distribution satisfies

$$\partial_{\tilde z}\kappa=\Lambda\left(\frac{\epsilon^{-\chi}}{1-\epsilon}\right)-1, \tag{B4}$$

which is subject to the bottom boundary condition $\epsilon(\tilde z_{\text{bottom}})=\epsilon_{\text{crit}}$.

At the top of the foam the hot wire bursts bubbles and the fluid from these bubbles either drains or is evaporated. Since the wire loop temperature is ~70 °C we make the assumption that evaporation is negligible and thus impose a no-flux boundary condition at the top, which is applying Eq. (B4) to the point $\tilde z_{\text{top}}$.

APPENDIX C: COUETTE SHEAR

We discuss wide-gap Couette shear and how the Herschel-Bulkley model [Eq. (7)] differs from Coussot's power-law model [Eq. (11)]. For both formulations the shear stress approaches $\dot\gamma^n$ at high shear rates, whereas at low shear rates the shear stresses approach their threshold values (τ_c for the power-law model and τ_y for the Herschel-Bulkley model). Naively, one might therefore expect only subtle differences, and indeed discerning differences between the two models is difficult. As we show, these expectations are born out and the differences only become apparent in the limit of slow angular velocities.

The dimensionless form of the Herschel-Bulkley model [Eq. (7)] is

$$\tilde\tau=1+\tilde{\dot\gamma}^n, \tag{C1}$$

where the stress is rescaled by τ_y and the time scale by $(\sigma k/R\tau_y)^{1/n}(\mu R/\sigma)$. The dimensionless form of the Coussot model [Eq. (11)] is

$$\tilde\tau=\tilde{\dot\gamma}^n, \tag{C2}$$

where the stress is rescaled by τ_c and the time scale by $(\sigma k_C/R\tau_c)^{1/n}(\mu R/\sigma)$. A natural choice for the length scale is the inner radius, $D_1/2$. The relationship between angular velocity and radius for the models follows from $\dot\gamma=r\partial_r\omega$ and the conservation of torque, $\tau(r)=\tau(r_0)(r/r_0)^{-2}$. The dimensionless ODE describing the angular velocity in terms of the shear stress at the inner cylinder for the Herschel-Bulkley is

$$\partial_{\tilde r}\tilde\omega_{\text{HB}}=\left(\frac{\tilde\tau(1)}{\tilde r^2}-1\right)^{1/n}\tilde r^{-1} \tag{C3}$$

and for the Coussot model is

$$\partial_{\tilde r}\tilde\omega_{\text{C}}=\tilde\tau(1)^{1/n}\tilde r^{-2/n-1}. \tag{C4}$$

For both models the no-slip condition enforces zero angular velocity at the outer cylinder, $\tilde D/2$, and the threshold stress condition imposes zero angular velocity when

$\tilde{\tau}(1)/\tilde{r}^2 \le 1$. Therefore the shear band only extends to the minimum of these two radii, $\tilde{r} \le \tilde{r}_c = \min[\tilde{\tau}(1)^{1/2}, \tilde{D}_2/2]$. The solution for the power law [Eq. (C4)] is

$$\tilde{\omega}_{\mathrm{C}} = \frac{n}{2}\tilde{\tau}(1)^{1/n}(\tilde{r}^{-2/n} - r_c^{-2/n}) = \begin{cases} \frac{n}{2}[(\tilde{\tau}(1)/\tilde{r}^2)^{1/n} - 1] & \text{for } \tilde{\tau}(1)^{1/2} \le \tilde{D}_2/2 \\ \frac{n}{2}\tilde{\tau}(1)^{1/n}[\tilde{r}^{-2/n} - (\tilde{D}_2/2)^{-2/n}] & \text{for } \tilde{\tau}(1)^{1/2} > \tilde{D}_2/2 \end{cases} \tag{C5}$$

and is shown as solid curves in Fig. 14(a) for three different shear stresses imposed by the rotating inner cylinder. The solution for the Herschel-Bulkley model [Eq. (C3)] involves a hypergeometric function of the second kind (whose formulation we omit here) and is shown as dashed curves. For a given applied shear stress and radial distance, the angular velocity predicted by the Herschel-Bulkley model is less. In the limit $\tilde{r} \to \tilde{r}_c$ the angular velocity ω_{C} drops off very steeply compared to ω_{HB}. For large applied shear stresses the angular velocity profiles are virtually indistinguishable. Figure 14(b) shows the dependence of the shear stresses on the angular velocity at the inner cylinder. Both models have the same asymptotic limits for large and small angular velocities, and the only difference is *how* the stresses approach unity with diminishing angular velocity. In the limit $\tilde{\omega} \to 0$ the power law approaches $\tilde{\tau} \to 1 + 2\tilde{\omega}$, whereas the Herschel-Bulkley model has a more gradual approach—see the inset of Fig. 14(a). For large angular velocities both models follow $\tilde{\tau} \propto \tilde{\omega}^n$, and by combining Eqs. (C4) and (C5) we obtain

$$\dot{\gamma} \approx \frac{2}{n}\omega, \tag{C6}$$

which is an approximation we make use of repeatedly to determine the capillary number in Secs. III C and III D.

It is important to note that although Coussot's power-law does have a cutoff minimum shear rate, $\dot{\gamma}_c$, it does *not* predict a cutoff in terms of the angular velocity of the inner cylinder. Thus at low angular velocities the approximation [Eq. (C6)] is violated.

[1] J. J. Bikerman, *Foams* (Springer, New York, 1973).

[2] *Foams: Theory, Measurements, and Applications*, edited by R. K. Prudhomme and S. A. Kahn (Dekker, New York, 1996).

[3] D. Weaire and S. Hutzler, *The Physics of Foam* (Oxford University Press, New York, 2000).

[4] G. Verbist and D. Weaire, Europhys. Lett. **26**, 631 (1994).

[5] S. A. Koehler, S. Hilgenfeldt, and H. A. Stone, Phys. Rev. Lett. **82**, 4232 (1999).

[6] D. J. Durian, D. A. Weitz, and D. J. Pine, J. Phys.: Condens. Matter **2**, SA433 (1990).

[7] D. Weaire and J. A. Glazier, Philos. Mag. Lett. **68**, 363 (1993).

[8] S. Hutzler and D. Weaire, Philos. Mag. Lett. **80**, 419 (2000).

[9] S. Hilgenfeldt, S. A. Koehler, and H. A. Stone, Phys. Rev. Lett. **86**, 4704 (2001).

[10] M. U. Vera and D. J. Durian, Phys. Rev. Lett. **88**, 088304 (2002).

[11] P. Stevenson, Colloids Surf., A **305**, 1 (2007).

[12] S. Jurine, S. Cox, and F. Graner, Colloids Surf., A **263**, 18 (2005).

[13] R. D. MacPherson and D. J. Srolovitz, Nature (London) **446**, 1053 (2007).

[14] R. Höhler and S. Cohen-Addad, J. Phys.: Condens. Matter **17**, R1041 (2005).

[15] D. M. Buzza, C. Y. Lu, and M. E. Cates, J. Phys. II **5**, 37 (1995).

[16] H. M. Princen and A. D. Kiss, J. Colloid Interface Sci. **112**, 427 (1986).

[17] A. Saint-Jalmes and D. J. Durian, J. Rheol. **43**, 1411 (1999).

[18] S. J. Neethling and J. J. Cilliers, Int. J. Min. Process. **72**, 267 (2003).

[19] L. L. Schramm, *Emulsions, Foams, and Suspensions: Fundamentals and Applications* (Wiley, New York, 2005).

[20] S. A. Khan and R. C. Armstrong, J. Non-Newtonian Fluid Mech. **22**, 1 (1986).

[21] A. Kraynik, Annu. Rev. Fluid Mech. **20**, 325 (1988).

[22] D. A. Reinelt and A. M. Kraynik, J. Rheol. **44**, 453 (2000).

[23] M. Durand and H. A. Stone, Phys. Rev. Lett. **97**, 226101 (2006).

[24] R. Hohler, Y. Y. C. Sang, E. Lorenceau, and S. Cohen-Addad, Langmuir **24**, 418 (2008).

[25] T. G. Mason, J. Bibette, and D. A. Weitz, Phys. Rev. Lett. **75**, 2051 (1995).

[26] T. G. Mason, J. Bibette, and D. A. Weitz, J. Colloid Interface Sci. **179**, 439 (1996).

[27] H. M. Princen and A. D. Kiss, J. Colloid Interface Sci. **128**, 176 (1989).

[28] S. Cohen-Addad, R. Höhler, and Y. Khidas, Phys. Rev. Lett. **93**, 028302 (2004).

[29] N. Denkov, Colloids Surf., A **263**, 129 (2005).

[30] N. D. Denkov, S. Tcholakova, K. Golemanov, K. P. Ananthapadmanabhan, and A. Lips, Phys. Rev. Lett. **100**, 138301 (2008).

[31] A. D. Gopal and D. J. Durian, Phys. Rev. Lett. **91**, 188303 (2003).

[32] At sufficiently high shear rates bubbles are split, which results in a finer foam.

[33] O. Reynolds, Philosophical Magazine Series 5 **50**, 469 (1885).

[34] S. J. Neethling, H. T. Lee, and J. J. Cilliers, J. Phys.: Condens. Matter **14**, 331 (2002).

[35] A. Saint-Jalmes, Y. Zhang, and D. Langevin, Eur. Phys. J. E **15**, 53 (2004).

[36] C. P. Gonatas, J. S. Leigh, A. G. Yodh, J. A. Glazier, and B. Prause, Phys. Rev. Lett. **75**, 573 (1995).

[37] A. Saint-Jalmes, Soft Matter **2**, 836 (2006).

[38] H. M. Princen and A. D. Kiss, J. Colloid Interface Sci. **105**, 150 (1985).

[39] R. Soller and S. A. Koehler, Phys. Rev. Lett. **100**, 208301 (2008).
[40] S. Rodts, J. C. Baudes, and P. Coussot, Europhys. Lett. **69**, 636 (2005).
[41] M. Durand, G. Martinoty, and D. Langevin, Phys. Rev. E **60**, R6307 (1999).
[42] P. Stevenson, Minerals Eng. **20**, 282 (2007).
[43] S. Tcholakova, N. D. Denkov, K. Golemanov, K. P. Ananthapadmanabhan, and A. Lips, Phys. Rev. E **78**, 011405 (2008).
[44] We restrict our discussion to positive quantities. For extending to negative values, we follow the convention that $x^n = \mathrm{sgn}(x)|x|^n$.
[45] H. M. Princen, M. P. Aronson, and J. C. Moser, J. Colloid Interface Sci. **91**, 160 (1983).
[46] F. P. Bretherton, J. Fluid Mech. **10**, 166 (1961).
[47] L. W. Schwartz and H. M. Princen, J. Colloid Interface Sci. **118**, 201 (1987).
[48] P. Coussot, Q. D. Nguyen, H. T. Huynh, and D. Bonn, Phys. Rev. Lett. **88**, 175501 (2002).
[49] P. Coussot, J. S. Raynaud, F. Bertrand, P. Moucheront, J. P. Guilbaud, H. T. Huynh, S. Jarny, and D. Lesueur, Phys. Rev. Lett. **88**, 218301 (2002).
[50] D. J. Durian, Phys. Rev. E **55**, 1739 (1997).
[51] V. Carrier, S. Destouesse, and A. Colin, Phys. Rev. E **65**, 061404 (2002).
[52] S. A. Koehler, H. A. Stone, M. P. Brenner, and J. Eggers, Phys. Rev. E **58**, 2097 (1998).
[53] P. Dankers, M. Harmsen, L. Brouwer, M. Van Luyn, and E. Meijer, Nature Mater. **4**, 568 (2005).
[54] H. Yan, A. Saiani, J. E. Gough, and A. F. Miller, Biomacromolecules **7**, 2776 (2006).
[55] J. M. Skotheim and L. Mahadevan, Science **308**, 1308 (2005).
[56] M. A. Rutgers, J. Z. Xue, E. Herbolzheimer, W. B. Russel, and P. M. Chaikin, Phys. Rev. E **51**, 4674 (1995).
[57] J. M. A. Hofman, H. J. H. Clercx, and P. P. J. M. Schram, Phys. Rev. E **62**, 8212 (2000).
[58] V. Carrier and A. Colin, Langmuir **18**, 7564 (2002).
[59] S. A. Koehler, S. Hilgenfeldt, and H. A. Stone, Langmuir **16**, 6327 (2000).